Aerodynamic and Acoustic analysis of a preliminary PrandtlPlane configuration within the framework of the PARSIFAL project

Marco Carini, Michaël Méheut, Laurent Sanders

Italian Association of Aeronautics and Astronautics
XXV International Congress
9-12 September 2019 | Rome, Italy

AERODYNAMIC AND ACOUSTIC ANALYSIS OF A PRELIMINARY PRANDTLPLANE CONFIGURATION WITHIN THE FRAMEWORK OF THE PARSIFAL PROJECT

M. Carini[1*], M. Méheut [1], L. Sanders[1]

[1] ONERA/DAAA, Université Paris-Saclay, F-92190 Meudon, France

*marco.carini@onera.fr

ABSTRACT

The present paper summarizes the main results obtained from the CFD analysis of a reference boxwing configuration designed during the initial phase of the PARSIFAL project, with focus on the assessment of its aerodynamic performance in the transonic regime. For such purpose, high-fidelity RANS computations have been carried out and a detailed inspection of the different drag sources, induced, wave and viscous drag components, is presented. In addition, preliminary results from the acoustic analysis of such innovative aircraft configuration are also discussed, concerning the impact of the engine location.

Keywords: Aerodynamics, Boxwing, PrandtlPlane, Far-field drag decomposition.

1 INTRODUCTION

The project PARSIFAL (Prandtlplane ARchitecture for the Sustainable Improvement of Future AirpLanes) [1], aims at defining the basis to improve the future air transport by evaluating the effects of introducing the innovative box-wing aircraft, called “PrandtlPlane” (PrP), into service. Indeed, it is well known from theoretical viewpoint that the PrP configuration presents the minimum induced drag among all possible wing architectures, as shown by Prandtl in 1924 [2] and proved in [3]. Notwithstanding the PrP can offer several additional advantages w.r.t. the traditional “tube and wing” configuration, also concerning engine integration, structure design and operability. However, at transonic cruise conditions, the appearance of strong shocks waves, in particular at the joined wing tips and at the fin, can seriously impact the overall PrP aerodynamic performance. A high-fidelity prediction and detailed analysis of the aerodynamic performance of such architecture is therefore necessary to properly assess the aforementioned expected benefits and determine the potential improvements that can be achieved by a refined design.

In the present work, an aerodynamic and acoustic analysis of the baseline PrandtlPlane (PrP) configuration (which defines the Milestone 1 of the PARSIFAL project, MS1) is presented. This baseline configuration is illustrated in Figure 1(a). In addition to this configuration, some analyses have also been performed on the isolated boxwing lifting system (Figure 1a) and on the updated PrP configuration showing the integration of the vertical tails (MS1.1), Figure 1 (b).

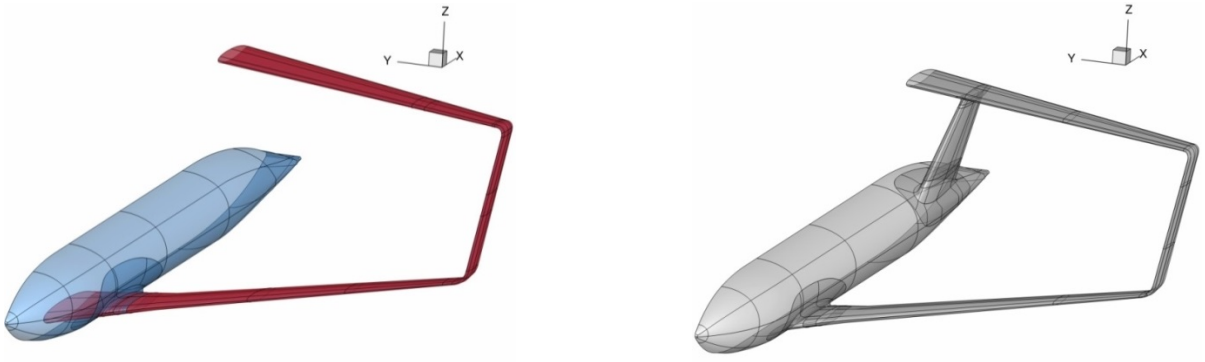

(a) (b)

Figure 1. Baseline PrP configurations (half-model): (a) MS1 (fuselage with integrated boxwing, light-blue) and MS1 isolated boxwing (red). (b) MS1.1 configuration featuring the integration of the vertical tail.

2 AERODYNAMIC ANALYSIS

2.1 Computational approach

RANS computations have been carried out by means of the in-house ONERA finite-volume solver *elsA* (ONERA-Airbus-Safran property) using an overset-grid approach. Body-fitted structured grids have been generated around the boxwing lifting-system, the fuselage, the vertical tail and around each corresponding intersection zone (collar grids). A Cartesian-octree background mesh has then been created automatically using the ONERA *Cassiopée* software library, with an extension of nearly 400 m (100 mean aerodynamic chords) away from the aircraft surface along the three spatial directions. The normal wall spacing is kept almost uniform everywhere with a size of ~5 μm, corresponding to a maximum y+~ 0.8 for the considered cruise conditions of Mach number M=0.79 and altitude of ~11 km. The steady RANS equations are supplemented by wall viscous boundary conditions on the solid surfaces, by appropriate far-field conditions on the external boundary of the background grid and by symmetry plane conditions at y=0 m (half-model simulation). The *Spalart-Allmaras* turbulence model with the QCR correction [4] is adopted and the Jameson scheme is used for the inviscid flux discretization. The resulting discretized equations are solved using pseudo-time iterations with dual time-stepping and multigrid acceleration to converge towards the desired mean flow solution at the best accuracy in terms of aerodynamic coefficients: as an example for cruise conditions at AoA=0.0 deg. (where no separations occur) the variation of the drag coefficient over the last 2000 iterations is as small as 0.01 d.c. (1 d.c. = 0.0001).

2.2 Detailed analysis at cruise conditions

The computed lift (CL(AoA)) and polar (CL(CD)) curves for both the isolated boxwing and the PrP configuration at cruise conditions, i.e. Mach number M=0.79 and Reynolds number $Re=25.86\times10^6$ (altitude 11.0 km), are illustrated in Figure 2(a) and Figure 2 (b), respectively. Note that the aerodynamic coefficients have been computed using the MS1 reference surface of 266.7 m^2. This explains the downward shift of the PrP lift curve compared to the isolated boxwing, due to the increase of the effective lifting surface (see Figure 1a) for this latter geometry, while keeping the same reference surface for the aerodynamic coefficient computation. The results show that, for both cases, the stall start to develop quite early, at an

incidence of ~2.5 deg, which limits the maximum lift coefficient around ~0.6-0.65. A far-field drag decomposition [5] has then been carried out for a fine performance assessment by evaluating the different drag contributions. Thanks to such analysis the polar curves of Figure 2(b) are decomposed according to the classical drag breakdown into the different physical sources: friction drag (CD_f), viscous pressure drag (CD_{vp}), wave drag (CD_w) and induced drag (CD_i). The results are illustrated in Figure 2(c). As expected, the contribution of the friction drag is almost insensitive to the lift coefficient and the shift of ~33 d.c. between the two curves is mainly due to the fuselage drag contribution. The wave drag is very small at negative values of AoA and gradually increases up to ~50 d.c. for CL greater than 0.6. A sudden drag rise is observed for the viscous pressure drag when CL increases over ~0.55, suggesting the onset of a large scale separation (which has been confirmed by the further inspection of the flow solution not shown here). At the same time, the wave drag rise is not as regular as expected. This is due to the fact that at low AoA, the main wave drag sources are located on the suction side of the lower wing tip (not shown here) whereas at high AoA, a separation occurs in this region, which prevents the development of the strong shock system previously observed.

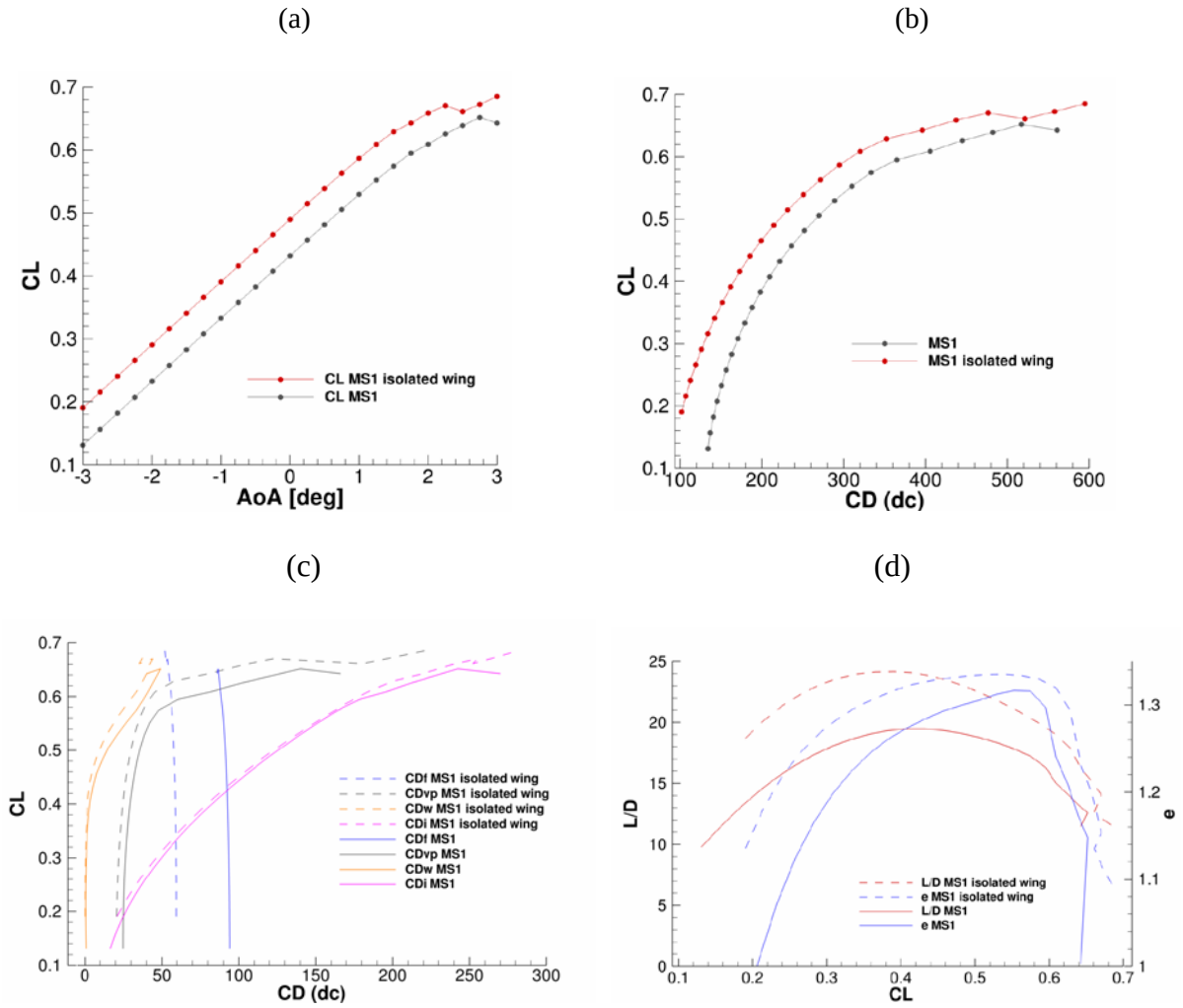

Figure 2. Aerodynamic coefficients computed for the MS1 PrP and the isolated boxwing: (a) Lift curve. (b) Polar curve.(c) Far-field decomposition. (d) Aerodynamic efficiency L/D and equivalent Oswald factor e as a function of CL for both the MS1 PrP and the corresponding isolated boxwing.

The overall aerodynamic efficiency, L/D, and the equivalent Oswald efficiency, *e* (which has been computed based on the extracted values of CD_i, the reference surface 266.7 m² and the span, 36 m) are illustrated in Figure 2(d) as a function of the lift coefficient CL. In particular, for both the MS1 configuration and the isolated boxwing the maximum efficiency is achieved close to the cruise design point, around CL ~ 0.4 and it drops from ~24.1 for the isolated boxwing to ~19.3 for the PrP configuration. As expected, for a boxwing architecture, the Oswald efficiency is greater than 1, with *e*=1.28 at the design cruise point (AoA=0.0 deg, CL=0.432).

2.3 Overall performance from low-speed to high-speed conditions

Extensive CFD RANS computations have been carried out in order to produce an aerodynamic database of the baseline PrP configuration for different flight conditions, ranging from subsonic to high transonic regimes at different altitudes, as required for aircraft mission analysis. These flight conditions are summarized in Table 1.

Flight Condition	Altitude ft	Mach
1	3000.0	0.3
2	10000.0	0.5
3	20000.0	0.65
4	30000.0	0.75
5	30000.0	0.8
6	30000.0	0.83
7	36000.0	0.79
8	36000.0	0.81
9	39000.0	0.83

Table 1. Flight conditions in terms of Mach numbers and altitudes for the MS1 PrP aerodynamic performance database generation.

The obtained lift, polar curves as well as the extracted wave drag polar, the total and the Oswald efficiency curves are illustrated in Figure 3. In particular, it can be observed that at up to CL ~0.5 the Oswald efficiency is almost independent of both Mach and altitude, which confirms the expected benefit offered by the boxwing architecture over a wide range of flight conditions in terms of induced drag. It is also observed that the wave drag becomes quite important by increasing Mach above 0.8, thus corroborating the choice of the value of Mach=0.79 for the cruise speed. This is furthermore supported by inspecting the total aerodynamic efficiency, reported in Figure 3(e). The maximum efficiency of ~21.36 is achieved at low speeds for CL ~0.47 and then gradually reduces as Mach increases, down to ~17.1 at Mach 0.83 for CL ~0.4, thus also featuring a shift of the maximum L/D towards lower values of the lift coefficient. Not surprisingly, as a consequence of the wave drag rise, by increasing Mach from 0.79 to 0.83 a severe efficiency drop of ~2.0 is observed.

3 ACOUSTIC ANALYSIS

The initial acoustic investigations in PARSIFAL have been dedicated to the analysis of the baseline configuration with a focus on the impact of (i) the vertical tail plane and (ii) the engine location.

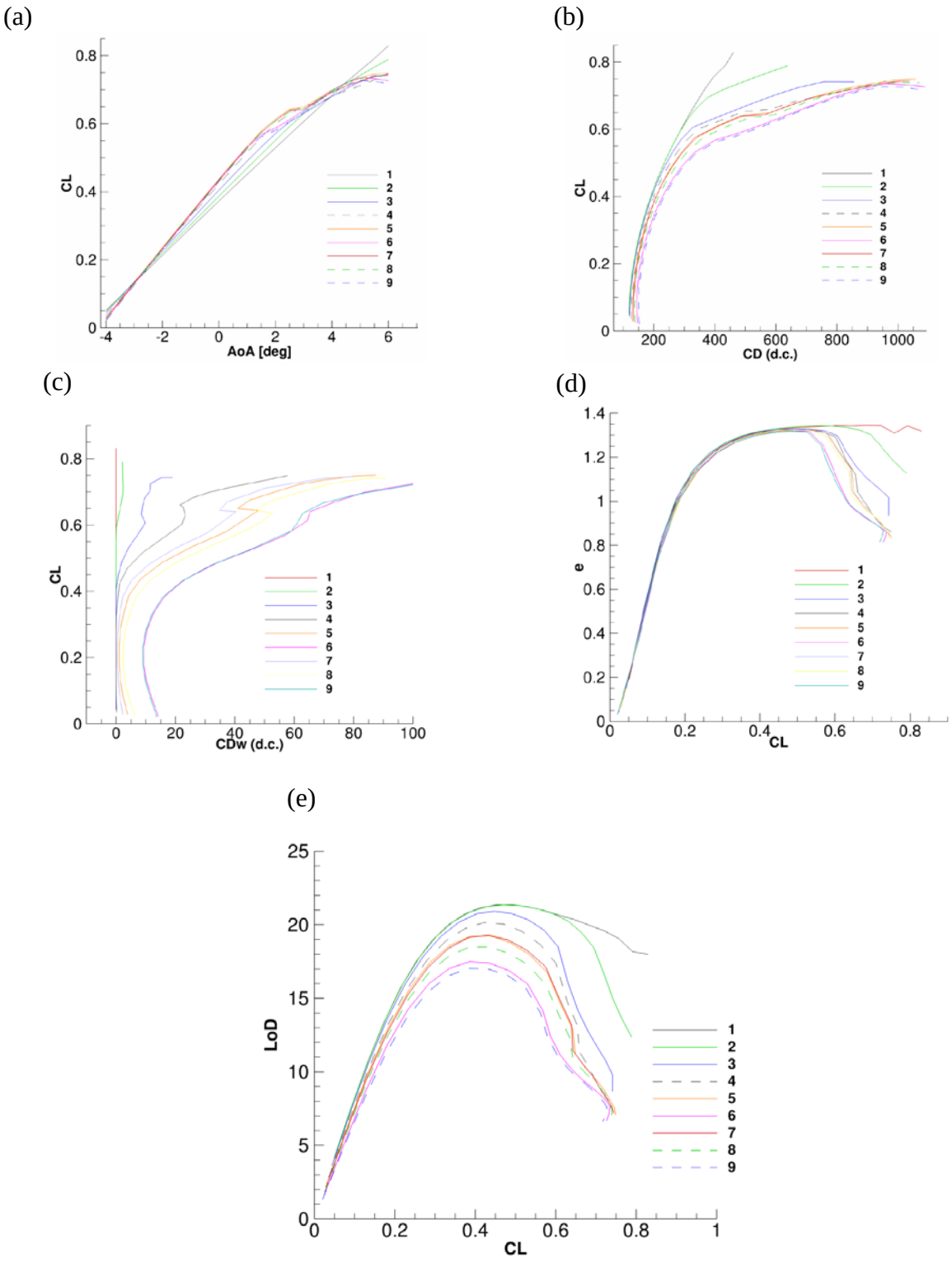

Figure 3. MS1 PrP aerodynamic performance for different flight conditions: (a) Lift curves. (b) Polar curves. (c) Wave drag polar curves. (d) Oswald efficiency curves. (e) Total aerodynamic efficiency.

3.1 Computational approach

3.1.1 Underlying assumptions

Several assumptions have been made in order to simplify the acoustic problem and obtain an affordable CPU cost for several computations corresponding to different engine locations. First of all, the engine noise is modeled as an acoustic point source and the engine is assumed to be dislocated (or isolated) from the airframe, thus no support of the engine is taken into account in the computations. In addition, several flow effects are not taken into account: (i) turbulence is out of the scope of such a study and (ii) given the low flow speed (Mach number lower than 0.25 for take-off or landing conditions), the convection effect of the flow can be neglected. As a first step, two others significant assumptions have been made: (i) the Doppler effect is neglected, so that the aircraft is modeled as motionless and (ii) the engine noise source is assumed to be *omni-directional* so that it can be modeled as a monopole, which results in a gross approximation of the noise emitted by a turbofan. The monopole source has a constant power emission at all the computed frequencies of the third-octave bands up to 1250 [Hz], based on the computed fan and jet broadband noise contributions during A320 flyover investigations at take-off carried out in a previous study [6]. Given the lower sound pressure levels of the noise beyond 1250 [Hz] and the increasing CPU cost for the computation at higher frequencies in our employed approach, noise frequencies beyond 1250 [Hz] are neglected in this preliminary study.

3.1.2 Computational method

Engine integration on aircraft requires an evaluation of the acoustic installation effect and the Boundary Element Method (BEM) can take into account complex geometries such as the one of a PrP configuration. The corresponding computational cost is proportional to the third power of the frequency of the acoustic source so its use is limited to low and medium frequencies. As stated previously, the performed computations have been focused on the frequency range of 20-1250 [Hz], which is dominating the engine noise emissions, and computations are run for the central frequencies of the third-octave bands included in this frequency range. Three surface meshes whose triangles size is 120, 70 and 35 mm and nodes number 94000, 273000 and 1088000, respectively, have been created for the computations. Figure 4 illustrates the general BEM approach in the case of engine noise. The engine acoustic source is assumed to be isolated from the scattering aircraft surface and its acoustic emission is modeled in the present case by a monopole.

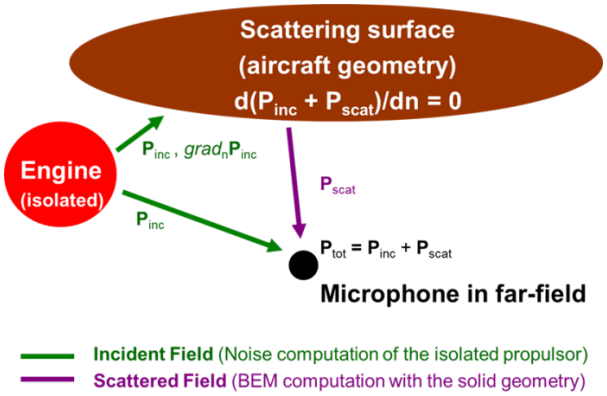

Figure 4. Sketch of the Boundary Element Method (BEM) approach for installed engine noise.

BEM is then employed to compute the pressure scattered by the aircraft surface from the incident field. The total pressure on the ground map is finally mirrored according to the y=0

plane in order to take into account two symmetric engines and the two pressure fields are summed without any coherence assumption.

3.1.3 Assessment methodology

A ground map under the motionless aircraft is then computed to assess the noise impact of the installed engine towards the ground, as illustrated in Figure 5. It is composed of 32000 microphones. A metric is also defined to take into account the scattering of the engine. It is named *Scattering Factor* (Z) and is defined as $Z = 10 * log_{10}\left\{\frac{\sum_f |P_{tot}(f)|^2}{\sum_f |P_{inc}(f)|^2}\right\}$, f being the central frequency of the third-octave bands from 20 to 1250 Hz.

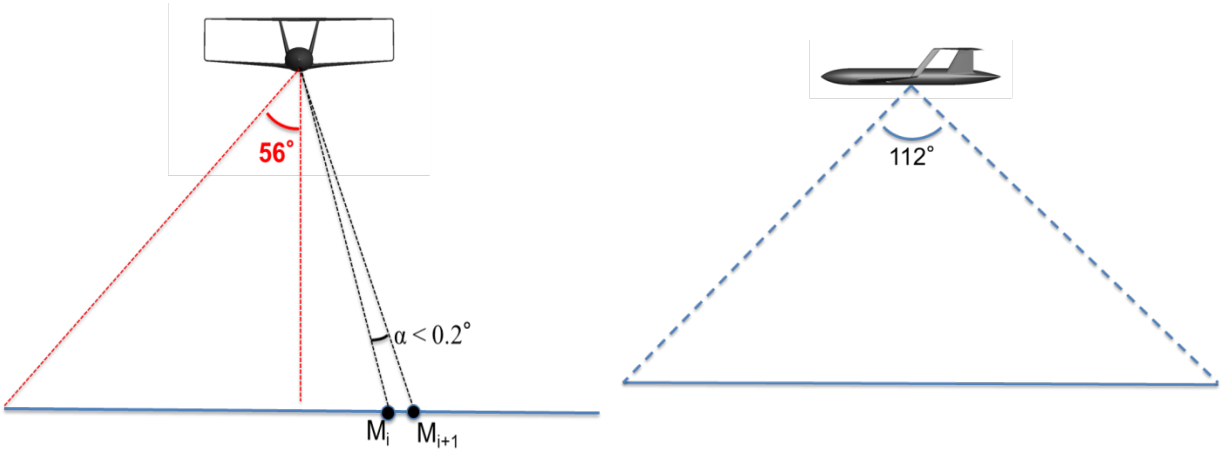

Front view *Side view*

Figure 5. Noise ground map definition (blue color) under the aircraft.

3.2 Aircraft configurations

The two different PrP configurations considered for computations, i.e. the MS1 and the MS1.1 (Figure 1), allow a preliminary assessment of the acoustic impact of the vertical tail plane and of the engine location. In particular, three different engine locations have been considered: a rear fuselage location, a positioning under the rear wing and a location above the front wing (Figure 6). Finally, by combining PrP geometries and engine locations, we obtain 6 different configurations whose names are listed in Table 2. More precisely, in the following, the acronym VTP is used to denote the MS1.1 configuration.

(a) (b) (c)

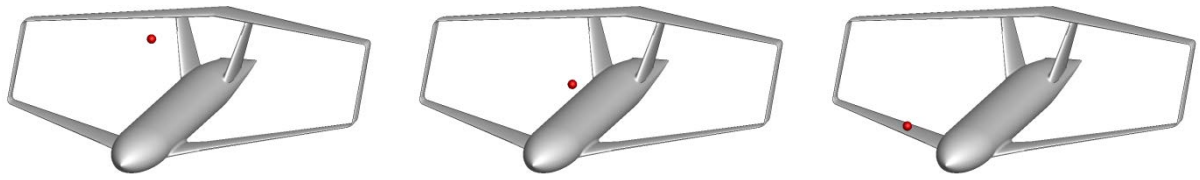

Figure 6. Considered engine locations: (a) under rear-wing location, (b) rear fuselage location and (c) above front-wing location. The engine acoustic source is represented by the red dot.

Configuration Names	
MS1_fuselage	*VTP_fuselage*
MS1_rearwing	*VTP_rearwing*
MS1_frontwing	VTP_frontwing

Table 2. Synthesis of the configuration names according to aircraft geometries and engine locations.

3.3 Results analysis

Given the longitudinal symmetry of the considered problem related to the two symmetric engine locations, the maps presented in Figure 7 are symmetric w.r.t. the y plane. In this figure, the two configurations with the engines above the wings are clearly mitigating the noise emission from the engines whereas the two configurations with the engines under the wings are the most disadvantageous. For this latter engine location only, the geometry with the vertical tails (*VTP*) induces a significant additional disadvantage. Table 3 focuses on the maximum of the scattering factor for each configuration. The worst configuration is logically the *VTP* with engine under the wing. Nonetheless, this result is qualified with the calculation of the amplification area S_a presented in Table 4. The amplification area is defined as the ratio between the area where noise amplification occurs, *i.e. Z>0*, and the map area. It is expressed in percent, *i.e.* $S_a = 100 * \frac{S(Z>0)}{S_{map}}$. It is shown that the two configurations with the engine close to the fuselage have the biggest amplification area, without any consideration of noise level ranking. This behaviour could be related to the large diffraction operated by the fuselage. By inspecting all the frequency computations, the most disadvantageous frequency can be extracted for each configuration according to the frequency scattering factor Z_f defined as $Z_f = 10 * log_{10}\left(\frac{|P_{tot}(f)|^2}{|P_{inc}(f)|^2}\right)$.

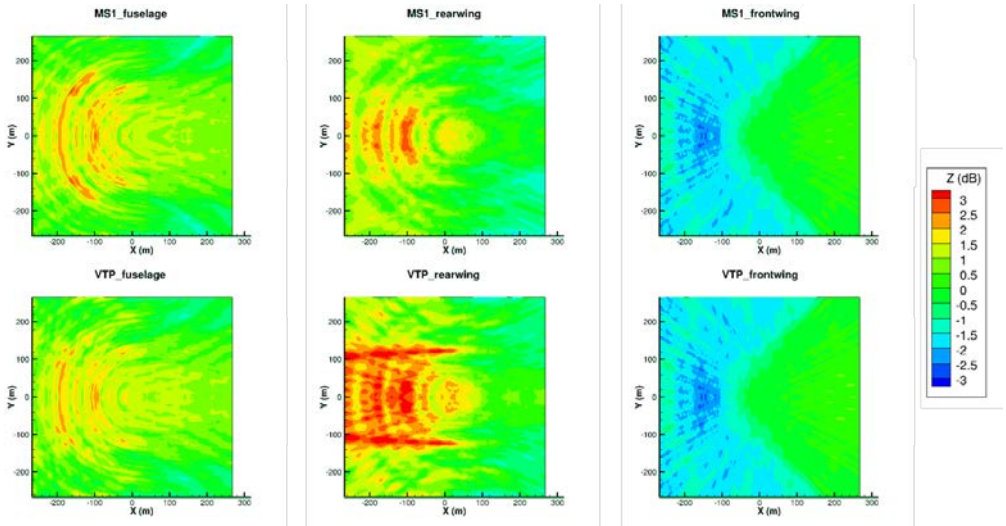

Figure 7. Scattering factor for all the considered configurations for acoustic analysis. Aircraft nose is oriented towards x>0 direction.

These frequencies are listed in Table 5. When the engine is above the front wing, the most disadvantageous frequency is very low (50 Hz) which corresponds to a wavelength of 6.8 m. For such wavelength, the shielding effect of the wing whose chord is lower than 3 m is unsignificant in the X direction whereas the diffraction on the 44-meters fuselage probably plays a dominant role in the amplification of the noise at point (-246,0). The engine position under the rear wing tends also to amplify the low frequencies (315-400 Hz) whereas the

engine position close to the fuselage tends to amplify the middle frequencies (1000-1250 Hz). These two different trends are tricky to analyse since the two engine positions are quite close and both involve reflection and diffraction effects. This aspect would deserve further analyses based on simpler geometries.

Configuration	MAX(Z), dB	X(m)	Y(m)
VTP_rearwing	**3.7**	**-174**	**-114**
MS1_fuselage	3	-162	-120
MS1_rearwing	2.9	-111	-27
VTP_fuselage	2.5	-162	-117
MS1_frontwing	**0.6**	**135**	**0**
VTP_frontwing	**0.6**	**135**	**0**

Table 3. Maxima of Z for all configurations and corresponding ground observer locations

.

Configuration	S_a (%)
MS1_fuselage	**81.7**
VTP_fuselage	**80.5**
VTP_rearwing	74.8
MS1_rearwing	63.5
VTP_frontwing	**17.4**
MS1_frontwing	**17.2**

Table 4. Ranking of configurations benefit according to the amplificated area S_a.

Configuration	Frequency (Hz)	Wavelength (m)	MAX(Z_f) (dB)	X (m)	Y (m)
VTP_rearwing	315	1.1	8	-75	-123
MS1_rearwing	400	0.9	7.2	-99	-12
VTP_fuselage	1250	0.3	7	-93	-255
MS1_fuselage	1000	0.3	6.8	-177	-126
MS1_frontwing	50	6.8	3.5	-246	0
VTP_frontwing	50	6.8	3.4	-249	0

Table 5. Maxima of frequency scattering factor for all configurations and corresponding ground observer locations.

4 CONCLUDING REMARKS

The aerodynamic and acoustic analyses of the baseline PrP configuration (mainly based on medium and high-fidelity CFD modelling) have been presented in this paper. Several interesting results have been obtained. In particular the expected benefits offered by the boxwing in terms of induced drag are confirmed over a wide range of flight conditions, from the low speed to the high transonic regime, the Oswald efficiency being almost independent

of the Mach number, with values of ~1.3 over the range of CL ~0.4-0.5. In addition, at design cruise conditions and with reference to the aspect ratio, which is fixed at 4.86, a quite high value of the aerodynamic efficiency is obtained with L/D=19.3. Notwithstanding, the CFD results have also highlighted the occurrence of severe shock wave at tip of the forward wing, with the onset of a large flow separation at relatively small incidence (not shown here), thus simultaneously reducing the maximum achievable lift while producing a strong drag rise.

On the acoustic side, preliminary analyses have shown that the engine location above the front wing is clearly relevant in terms of engine noise mitigation while positioning the engine at the rear of the aircraft (rear fuselage and under the rear wing) results disadvantageous. Further investigations, including higher-fidelity noise source modelling, will help in assessing the trade-off between these two configurations in terms of noise impact.

5 ACKNOWLEDGEMENTS AND REFERENCES

The present paper presents part of the activities carried out within the research project PARSIFAL (“Prandtlplane ARchitecture for the Sustainable Improvement of Future AirpLanes”), which has been funded by the European Union under the Horizon 2020 Research and Innovation Program (Grant Agreement n.723149).

REFERENCES

[1] A. Frediani, V. Cipolla, V. Binante, K. Abu Salem, M. Maganzi. PARSIFAL PROJECT: A BREAKTHROUGH INNOVATION IN AIR TRANSPORT in *“Proceedings of XXIV AIDAA International Conference”*, 18-22 September 2017, Palermo & Enna (Italy).

[2] L. Prandtl, “Induced drag of multiplanes", NACA Technical Note, no. 182, 1924.

[3] Frediani A. & Montanari G., *“Best wing system: An exact solution of the Prandtl's problem”*. In G. Buttazzo and A. Frediani Ed., Variational Analysis and Aerospace Engineering. Page. 181-211.

[4] Spalart, P. R., "Strategies for Turbulence Modelling and Simulation", *International Journal of Heat and Fluid Flow*, **21** , pp. 252-263(2000).

[5] D. Destarac, *“Drag Extraction from Numerical Solutions to the Equations of Fluid Dynamics: the Far-field “Philosophy”.”*, 43ème Congrès d’Aérodynamique Appliquée de la 3AF, Maîtrise de la traînée et de l’impact sur l’environnement, Poitiers (France), 10-12 Mars 2008.

[6] Legriffon, I., *“Aircraft noise modelling and assessment in the IESTA program with focus on engine noise”*, *The 22nd International Congress on Sound and Vibration*, 12-16 July 2015, Florence (Italy)